

Reduced model prediction of electron temperature profiles in microtearing-dominated National Spherical Torus eXperiment plasmas

S. M. Kaye, W. Guttenfelder, R. E. Bell, S. P. Gerhardt, B. P. LeBlanc, and R. Maingi

Citation: *Physics of Plasmas* (1994-present) **21**, 082510 (2014); doi: 10.1063/1.4893135

View online: <http://dx.doi.org/10.1063/1.4893135>

View Table of Contents: <http://scitation.aip.org/content/aip/journal/pop/21/8?ver=pdfcov>

Published by the [AIP Publishing](#)

Articles you may be interested in

[Resistive magnetohydrodynamic simulations of helicity-injected startup plasmas in National Spherical Torus eXperiment](#)

Phys. Plasmas **20**, 092510 (2013); 10.1063/1.4821977

[Simulations of drift resistive ballooning L-mode turbulence in the edge plasma of the DIII-D tokamaka\)](#)

Phys. Plasmas **20**, 055906 (2013); 10.1063/1.4804638

[Characterization and parametric dependencies of low wavenumber pedestal turbulence in the National Spherical Torus Experimenta\)](#)


Phys. Plasmas **20**, 055903 (2013); 10.1063/1.4803913


[Scaling of linear microtearing stability for a high collisionality National Spherical Torus Experiment discharge](#)

Phys. Plasmas **19**, 022506 (2012); 10.1063/1.3685698


[Studies of improved electron confinement in low density L-mode National Spherical Torus Experiment discharges](#)

Phys. Plasmas **13**, 092511 (2006); 10.1063/1.2355664

A collection of five pieces of industrial vacuum equipment from Pfeiffer Vacuum. From top-left to bottom-right: a red rectangular turbopump, a cylindrical stainless steel turbopump, a white rectangular turbopump, a red cylindrical turbopump with a long metal shaft, and a large, complex stainless steel chamber or component.

 Vacuum Solutions from a Single Source

- Turbopumps
- Backing pumps
- Leak detectors
- Measurement and analysis equipment
- Chambers and components

PFEIFFER  **VACUUM**

Reduced model prediction of electron temperature profiles in microtearing-dominated National Spherical Torus eXperiment plasmas

S. M. Kaye,^{a)} W. Guttenfelder, R. E. Bell, S. P. Gerhardt, B. P. LeBlanc, and R. Maingi
Princeton Plasma Physics Laboratory, Princeton University, Princeton, New Jersey 08543, USA

(Received 30 May 2014; accepted 30 July 2014; published online 14 August 2014)

A representative H-mode discharge from the National Spherical Torus eXperiment is studied in detail to utilize it as a basis for a time-evolving prediction of the electron temperature profile using an appropriate reduced transport model. The time evolution of characteristic plasma variables such as β_e , ν_e^* , the MHD α parameter, and the gradient scale lengths of T_e , T_i , and n_e were examined as a prelude to performing linear gyrokinetic calculations to determine the fastest growing micro instability at various times and locations throughout the discharge. The inferences from the parameter evolutions and the linear stability calculations were consistent. Early in the discharge, when β_e and ν_e^* were relatively low, ballooning parity modes were dominant. As time progressed and both β_e and ν_e^* increased, microtearing became the dominant low- k_θ mode, especially in the outer half of the plasma. There are instances in time and radius, however, where other modes, at higher- k_θ , may, in addition to microtearing, be important for driving electron transport. Given these results, the Rebut-Lallia-Watkins (RLW) electron thermal diffusivity model, which is based on microtearing-induced transport, was used to predict the time-evolving electron temperature across most of the profile. The results indicate that RLW does a good job of predicting T_e for times and locations where microtearing was determined to be important, but not as well when microtearing was predicted to be stable or subdominant. © 2014 AIP Publishing LLC.

[<http://dx.doi.org/10.1063/1.4893135>]

I. INTRODUCTION

The use of reduced transport models in the plasma core is critical to rapid assessment and prediction of operational scenarios in present and future devices. The necessary validation studies of these models as precursors to their use in predicting performance aids in developing an understanding of the processes controlling transport in present-day devices. Fundamental non-linear gyrokinetic calculations that determine the microturbulence driving the plasma transport and the transport levels^{1–6} are time and computer intensive, especially if they span multi-scales (from electron to ion-scale turbulence) and realistic mass ratios.⁷ Therefore, using reduced models, either analytic or numerical-based, is the desired option for the aforementioned studies. The discussion in this paper will focus on models in the plasma core ($r/a \leq 0.8$).

Reduced transport models of one form or another have been around for years, if not decades. Some representative examples include the Coppi-Tang-Redi model based on electron temperature profile “resiliency.”⁸ This model, with ad-hoc electron thermal diffusivity, χ_e profile adjustments, has been benchmarked against Alcator C-Mod data⁹ and was the basis for assessing ITER performance under a range of heating and current drive scenarios.¹⁰ Other reduced models used for predicting ITER performance include Bohm-gyroBohm¹¹ and the Multi-Mode model.¹² The latter model

combines a number of individual models covering ion to electron-scale turbulence-driven transport.

The GLF23 (Ref. 13) model and its successor TGLF,¹⁴ are numerically based and were developed from fits to the parameter variations of transport levels calculated through non-linear GYRO runs of a standard DIII-D discharge. Implicit in these models is a treatment of the ExB shear suppression of the turbulence that drives transport in both the ion and electron channels. These models, especially TGLF, have been well-validated with respect to DIII-D H-mode and Hybrid discharges,¹⁵ although the model does lead to a significant underestimate of both the turbulence and transport in the outer regions of DIII-D L-mode discharges.¹⁶ The source of this difference is presently under investigation. A key feature of GLF23 and TGLF is the ability to predict not only the energy transport but also the transport of particles and momentum as well. This capability has allowed for first generation full simulations of ITER performance in H-mode and Hybrid scenarios.^{17,18}

The GLF23 and, even while validation studies are ongoing, the TGLF models have been found to predict ion and electron transport and temperatures accurately in conventional aspect ratio ($R/a = 2.5–3$, where R is major radius and a is minor radius) tokamaks where electrostatic instabilities such as the Ion Temperature Gradient/Trapped Electron Mode (ITG/TEM) or Electron Temperature Gradient (ETG) modes are dominant.¹⁵ The Spherical Torus or Tokamak (ST) presents a greater challenge. For one, the aspect ratio in STs such as National Spherical Torus eXperiment (NSTX) or Maga-Amp Spherical Tokamak (MAST) is approximately one-half that in DIII-D, with the operational

^{a)} Author to whom correspondence should be addressed. Electronic mail: skaye@pppl.gov

regime in DIII-D being the basis for the development of GLF23 and TGLF. Second, STs operate at low toroidal magnetic field, B_T ($\sim 1/10$ that in conventional aspect ratio devices), and thus higher volume-averaged toroidal beta, $\langle \beta_T \rangle$, where electromagnetic effects are important. Here, $\beta_T \propto P/B_T^2$, where P is the plasma pressure. In ST plasmas at high $\langle \beta_T \rangle$ and relatively high collisionality, the microtearing mode¹⁹ has been predicted to be unstable in the plasma core,^{20–23} and non-linear GYRO calculations of NSTX plasmas show that the resulting χ_e due to microtearing turbulence both agrees with that inferred at a particular experimental condition and varies strongly with collisionality in a manner consistent with the strong collisionality dependence of normalized confinement observed in NSTX.^{24–26} The challenge for these microtearing unstable plasmas, then, is to identify a reduced transport model that is able to predict electron temperatures in this unique ST parameter regime in order to have confidence in extrapolation to future, lower collisionality STs such as NSTX-Upgrade²⁷ and a Fusion Nuclear Science Facility (FNSF),²⁸ where microtearing may be unstable.

This paper is organized in the following manner. Temporal parameter variations of a representative NSTX H-mode discharge are presented in Sec. II, with the associated discussion motivated by what these variations indicate in terms of expected plasma stability to microtearing and other microturbulence. In Sec. III, linear growth rates, real frequencies, and mode structures are determined using the GYRO code. Not surprisingly, the stability characteristics are consistent with the expectations from the parameter variations studied in Sec. II. The examination of parameter variations and determination of the unstable modes are critical to understanding the electron temperature, T_e , profile evolution predictions based on a reduced model of microtearing transport^{29,30} performed in Sec. IV. It is important to establish the guidelines for where and when agreement with such a reduced model is expected, and where and when it is not. Model predictions show good agreement with the experimentally measured T_e profiles for locations and times where microtearing is predicted to be unstable, but agreement is not good for times and locations when microtearing is predicted to be stable or subdominant. A comparison is also made between the measured electron stored energy and that given by the model predictions. A summary and discussion of future work are given in Sec. V.

II. DISCHARGE DESCRIPTION AND PARAMETER EVOLUTION

Time traces for the representative discharge used for this study are plotted in Fig. 1. The discharge, NSTX shot number 120967, is an H-mode which was taken from a confinement study consisting of I_p and B_T scans in plasmas using helium glow discharge cleaning plus boronization for wall conditioning. No lithium wall conditioning was used during this period of operation. It was from this collection of discharges that the strong increase in normalized confinement with decreasing collisionality, $B\tau_e \sim \nu_e^{*-0.97}$ was first identified.²⁵ This particular discharge had a plasma current I_p of 0.7 MA, a toroidal field B_T of 0.35 T, a deuterium neutral

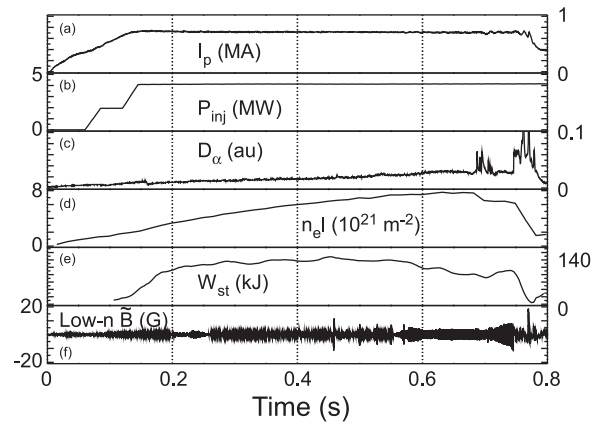


FIG. 1. Discharge evolution for NSTX shot 120967, the representative discharge used in this study. Shown from the top panel down are plasma current, injected neutral beam power, lower divertor D_α emission, line-integral electron density, total stored energy, and low frequency $n = 1$ MHD activity.

beam (NB) heating power of ~ 4 MW into a Lower Single Null (LSN) deuterium plasma with elongation, κ , ~ 2.2 and plasma density up to $6 \times 10^{19} \text{ m}^{-3}$. All of these discharges exhibited small, high frequency Edge Localized Modes (ELMs). This discharge was one of the highest collisionality discharges in the scans, which consisted of varying I_p from 0.7 to 1.1 MA and B_T from 0.35 to 0.55 T in the same geometry and with the same heating power and density. In the discharge shown in the figure, the electron temperature and density were measured by a 20-point Thomson scattering diagnostic every 16 ms, the (carbon) ion temperature, toroidal rotation, and impurity density by a 51-point charge exchange recombination spectroscopy diagnostic every 10 ms, and the magnetic field pitch (i.e., B_p/B_T , which yielded local q via magnetic equilibrium reconstructions) by a 12-point motional Stark effect diagnostic also every 10 ms. Since the time of this discharge (2006), the radial resolution of the motional Stark effect and Thomson scattering diagnostics has increased.

The discharge plasma current and injected neutral beam power are shown in the top two panels (a) and (b) in Fig. 1, with the injected power reaching its maximum of ~ 4 MW by $t = 0.14$ s. The plasma current remained constant essentially out to 0.7 s. As can be seen in the lower divertor D_α trace (Fig. 1(c)), the discharge transitioned from L- to H-mode at $t = 0.16$ s, and exhibited small, type V ELMs until $t = 0.68$ s. The line-integral electron density (Fig. 1(d)) increased throughout the discharge, primarily from beam fueling, and the stored energy (Fig. 1(e)) remained constant until just after 0.58 s, when it started a slow decrease with time in response to an increase in low-frequency $n = 1$ oscillations at that time (Fig. 1(f)). The spikes in the D_α trace at $t = 0.68$ s represented a possible transition back to the L-mode, and the discharge terminated in response to MHD mode locking starting at $t = 0.74$ s. The behavior of this discharge is typical of most NSTX plasmas during this operational period. Times of interest for the global confinement studies²⁵ were taken during periods of low MHD activity ($t \sim 0.5$ s), although for the study to be presented here, data and results will be shown at the following times: $t = 0.2, 0.3, 0.4, 0.5, 0.6,$ and 0.7 s.

The time evolution of the electron temperature T_e , the ion temperature T_i , and the electron density n_e profiles is

shown in Figs. 2(a)–2(c), where the respective profiles are plotted every 0.1 s from $t = 0.2$ to 0.7 s. The profiles are plotted as a function of $x = [\Phi/\Phi_a]^{0.5}$, where Φ is local toroidal flux and Φ_a is toroidal flux at the boundary. These profiles are taken from a TRANSP run into which the spline-fitted measured data were input, symmetrized, and in the case of n_e , in-out averaged about the magnetic axis. For the analysis to be shown here, single time slices from the TRANSP output were used; however, the input spline fits were time-averaged over ± 25 ms. The information in the TRANSP run was used as a basis for the examination of the local parameter variations and input to the linear stability GYRO calculations to be presented later in this work. A more comprehensive discussion of the inputs to and treatment in TRANSP can be found in Kaye *et al.*^{24,25} and references therein.

The T_e profiles shown in Fig. 2(a) are remarkably self-similar from $x = 0.4$ to the boundary for all times shown. Some variation in the profile shape for $x \leq 0.4$ is seen at early times (0.2–0.4 s), but outside of that radius the profile is seen to retain its shape but secularly decrease in magnitude over time as the density in the discharge increases (see Fig. 1(d)). The T_i profiles (Fig. 2(b)) show self-similarity, decreasing in magnitude from 0.2 to 0.5 s, but then exhibit a significant drop inside of $x = 0.4$ for 0.6 and 0.7 s. The T_i data beyond $x \simeq 0.85$ are not shown due to large uncertainties. Inside of $x = 0.85$, the data typically have uncertainties in the 2%–3% range, while outside of this radius (and below 100 eV), the uncertainties are between 5% and 10%. An additional uncertainty for T_i is due to the deviation of the data from the spline fit. This is typically another 1%–3%, except for the earliest two times when it was from 4%–10%. Representative error bars combining estimates from both sources of error are shown in Fig. 2(b). The density profiles (Fig. 2(c)) show the typical ear associated with the H-mode at $x = 0.6$ – 0.8 . The ear, caused by carbon fueling in NSTX, moves slightly inward with time. The ear disappears in the last profile at $t = 0.7$ s, reverting back to an L-mode profile shape in the outer region in response to the probable H-L back transition at $t = 0.68$ s. The uncertainties in the T_e and n_e profiles are approximately 2%–3% across the profile. The

deviation of the data from the spline fit for T_e and n_e is another 1%–3%, and representative error bars from the combined uncertainties are shown in the figure. It is of interest to note that even after this time, the T_e profile retains its self-similar shape. The typical electron energy confinement time during this period ($t = 0.68$ – 0.7 s) is 12–16 ms, so if there were a completely different transport mechanism controlling the T_e profile after the H-L transition than before, profile changes would most likely have been observable by $t = 0.7$ s.

Much can be surmised concerning the controlling microturbulence-driven electron transport over the entire time range by tracking the time evolution of parameters believed to represent the importance of various turbulent modes. For tracking these parameters, three radial locations were chosen, $x = 0.35$, 0.50 , and 0.65 , and the parameter evolution was studied along the same lines as that shown in Fig. 1 in Guttenfelder *et al.*²⁶ The first set of parameters that will be examined are the electron beta, β_e , and collisionality, ν_e^* , which are plotted against each other in Fig. 3(a). Here, β_e is the electron pressure normalized to the magnetic pressure and the collisionality is $\propto n_e Z_{\text{eff}}/T_e^2$. Each line in the figure is color-coded according to radius, and the lines represent the temporal evolution of the parameters from 0.2 to 0.7 s. The arrows on each line indicate the direction of advancing time, and the points represent the actual data values every 0.1 s in the time range of interest. At the earliest times, both β_e and ν_e^* are relatively low at all three radii, indicating the lower β modes such as ballooning-parity ITG/TEM/ETG modes may be most important. As time advances, both β_e and ν_e^* increase into regimes where the Kinetic Ballooning Mode (KBM), at high β_e and low ν_e^* , and especially the microtearing mode (high β_e and high ν_e^*) may be important (see Fig. 1(a) in Guttenfelder *et al.*²⁶). β_e drops at $t = 0.7$ s for $x = 0.50$ and especially for $x = 0.65$, indicating the possible importance of the ITG/TEM/ETG modes once again.

The MHD parameter $\alpha \propto -(q^2 R_0/B)dP/dr$ is plotted against $\beta_e R/L_{T_e}$ in Fig. 3(b). The parameter α reflects the importance of the KBM, while $\beta_e R/L_{T_e}$ is used as an identifier for microtearing, which depends both on β_e and R/L_{T_e} . Microtearing modes generally occur at high values of this parameter, while KBMs occur at high values of α . As can be

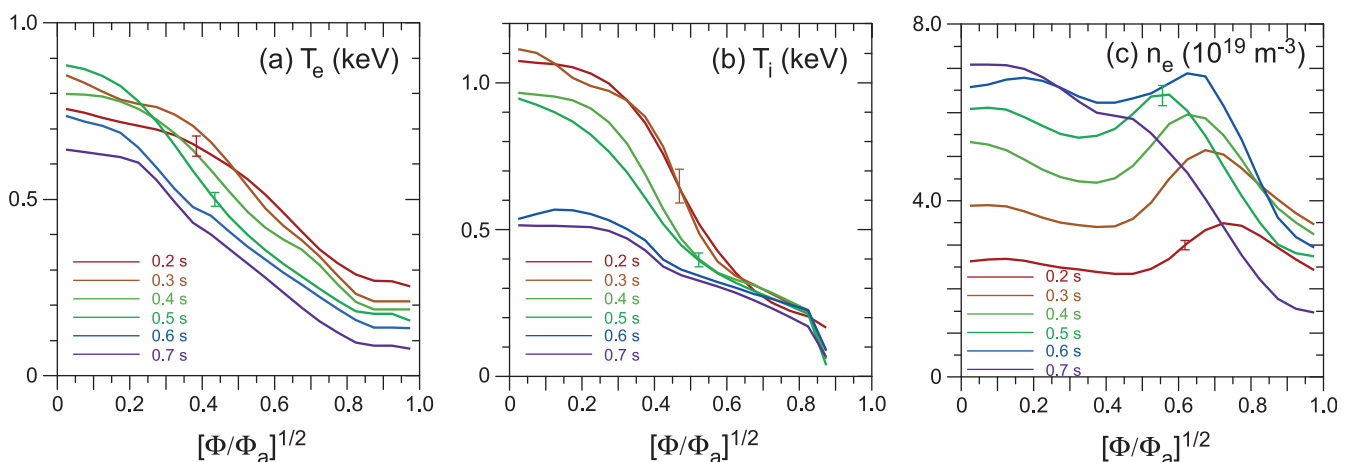


FIG. 2. Electron temperature, ion temperature, and electron density profiles taken every 0.1 s from 0.2 to 0.7 s plotted as a function of the radial coordinate $x = [\Phi/\Phi_a]^{0.5}$, where Φ is local toroidal flux, and Φ_a is toroidal flux at the boundary.

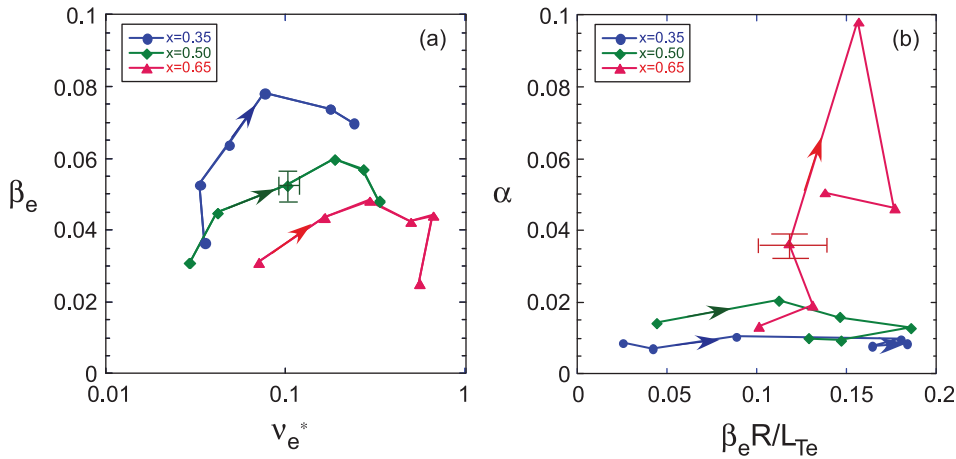


FIG. 3. (a) The time evolution of the electron beta vs collisionality for the three radial locations of interest and (b) time evolution of the MHD α parameter vs $\beta_e R/L_{Te}$.

seen in Fig. 3(b), the $\beta_e R/L_{Te}$ values for $x=0.35$ and 0.50 increase in time at relative constant α into a possible microtearing regime, while values at $x=0.65$ mostly reside at the highest $\beta_e R/L_{Te}$, also in the possible microtearing regime. (Note that the word “possible” is being used, since these parameter variations are used as guides; more definitive conclusions about which modes exist cannot be made until at least linear gyrokinetic stability estimates are made, and these are presented in Sec. III.) For $x=0.65$, the $t=0.5$ s point also resides at its maximum α value, indicating the potential for the existence of mixed modes at this time and location.

Finally, the evolution of the normalized profile gradients are plotted in Figs. 4(a) and 4(b). R/L_{n_e} is plotted against R/L_{Te} in Fig. 4(a), while it is plotted against R/L_{Ti} in Fig. 4(b). The normalized temperature gradients especially reflect the drive terms for the microtearing/ETG and ITG modes, respectively. Note that the density profile can be inverted, as indicated in Fig. 2(c) and by the negative values of R/L_{n_e} . Relatively low values of R/L_{n_e} and R/L_{Te} are seen for $x=0.35$ and $x=0.5$ at the earliest times, while R/L_{Te} is larger for $x=0.65$ then, indicating the possibility of electrostatic ∇T_e -driven modes (β_e is low at this time as is seen in Fig. 3(a)). The ∇T_e drive at $x=0.35$ and 0.5 increases with advancing time, as it does at $x=0.65$, where, for this radius, ∇n_e also increases. The highest R/L_{n_e} points at $x=0.65$ also exhibit relatively large values of α (see Fig. 3(b)), supporting the speculation that mixed modes (microtearing and KBM)

may co-exist at these locations at these times (especially for $t=0.5$ s). Fig. 4(b) shows very large R/L_{Ti} at the earliest times for $x=0.50$ and 0.65 , coupled with large inverted density gradients, indicating the potential for ∇T_i -driven electrostatic (low β) modes. The ∇T_i drive becomes smaller as the discharge evolves in time.

To summarize these trends, the following picture emerges. At the earliest times, low- β electrostatic modes driven by ∇T_e and especially by ∇T_i are expected to be important at $x=0.50$ and 0.65 . As time advances, and both β_e and ν_e^* increase, microtearing is expected to become important at all three radii. At $x=0.65$, R/L_{n_e} and α become large at later times, suggesting the possibility for microtearing and KBMs to co-exist at these times. Also at later times, the ∇T_e drive becomes important at $x=0.65$, while β_e drops at $t=0.7$ s at this radius, suggesting the potential for low- β , electrostatic ETG modes to exist.

III. LINEARLY UNSTABLE MODES

In this section, the existence of various modes will be investigated from results of linear stability calculations using the GYRO code.¹ Plasma profiles and equilibria taken from TRANSP interpretive analysis were input into GYRO, and calculations were performed across a large range of $k_\theta \rho_s$ for the six times and all three radial locations. The $k_\theta \rho_s$ ranged from 0.2 to 40 in a relatively coarse grid, with the following values evaluated: $k_\theta \rho_s = 0.2, 0.4, 0.6, 0.8, 1, 2, 4, 6, 8, 10,$

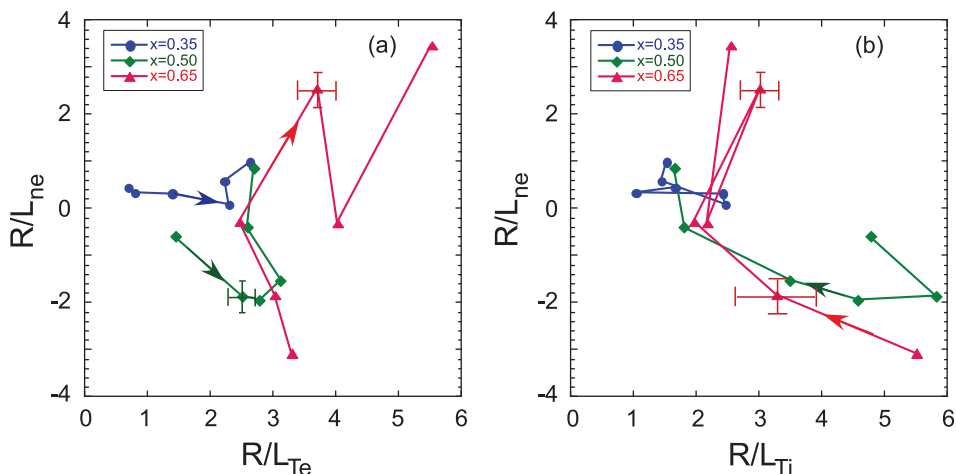


FIG. 4. (a) The time evolution of the normalized electron density gradient vs normalized electron temperature gradient and (b) time evolution of the normalized electron density gradient vs normalized ion temperature gradient.

20, 40. A Miller (analytic)³¹ equilibrium was used for all calculations with a strict convergence criterion of $1.e-3$.

In Figs. 5(a)–5(f), the results of this linear stability analysis for $x=0.65$ at the six different times are shown. The results for only this radius will be presented graphically, although the results for $x=0.35$ and 0.50 will be summarized at the end of the section. In each panel, the real frequency (dashed line, open points, left ordinate) and growth rate (solid line, solid points, right ordinate), normalized to the local value of c_s/a , are shown as a function of $k_\theta \rho_s$ for the fastest growing mode. The results are color-coded with red indicating ballooning parity (e.g., ITG/TEM/ETG/KBM) and blue indicating tearing parity (e.g., microtearing). Normalized real frequencies > 0 correspond to the electron direction while those < 0 correspond to the ion direction. The horizontal shaded region represents the absolute value of the ExB shearing rate given by $\gamma_E = -(r/q)d\Omega/dr$ normalized to the local value of c_s/a . Here, Ω is the toroidal rotation

frequency, which is the overwhelmingly dominant contribution to the ExB shear in these NSTX plasmas.

A sharp switch from tearing to ballooning parity modes is seen to occur over a narrow range in $k_\theta \rho_s$ in some cases to be shown, and this reflects a close competition between the two modes for dominance. Thus, while the fastest growing mode is the dominant mode, the subdominant mode may be strong enough as well to influence the transport level. Only non-linear calculations would include the influence of all unstable modes, and while these are underway, a comprehensive non-linear-based study is beyond the scope of this paper.

Ballooning parity modes in both the ion and electron directions are seen at the earliest time, $t=0.2$ s (Fig. 5(a)), with the linear growth rates of the ion modes ($k_\theta \rho_s \leq 4$) exceeding the ExB shearing rate by over a factor of two. Electron direction modes at higher $k_\theta \rho_s$ have linear growth rates that are approximately one-half the ExB shearing rate.

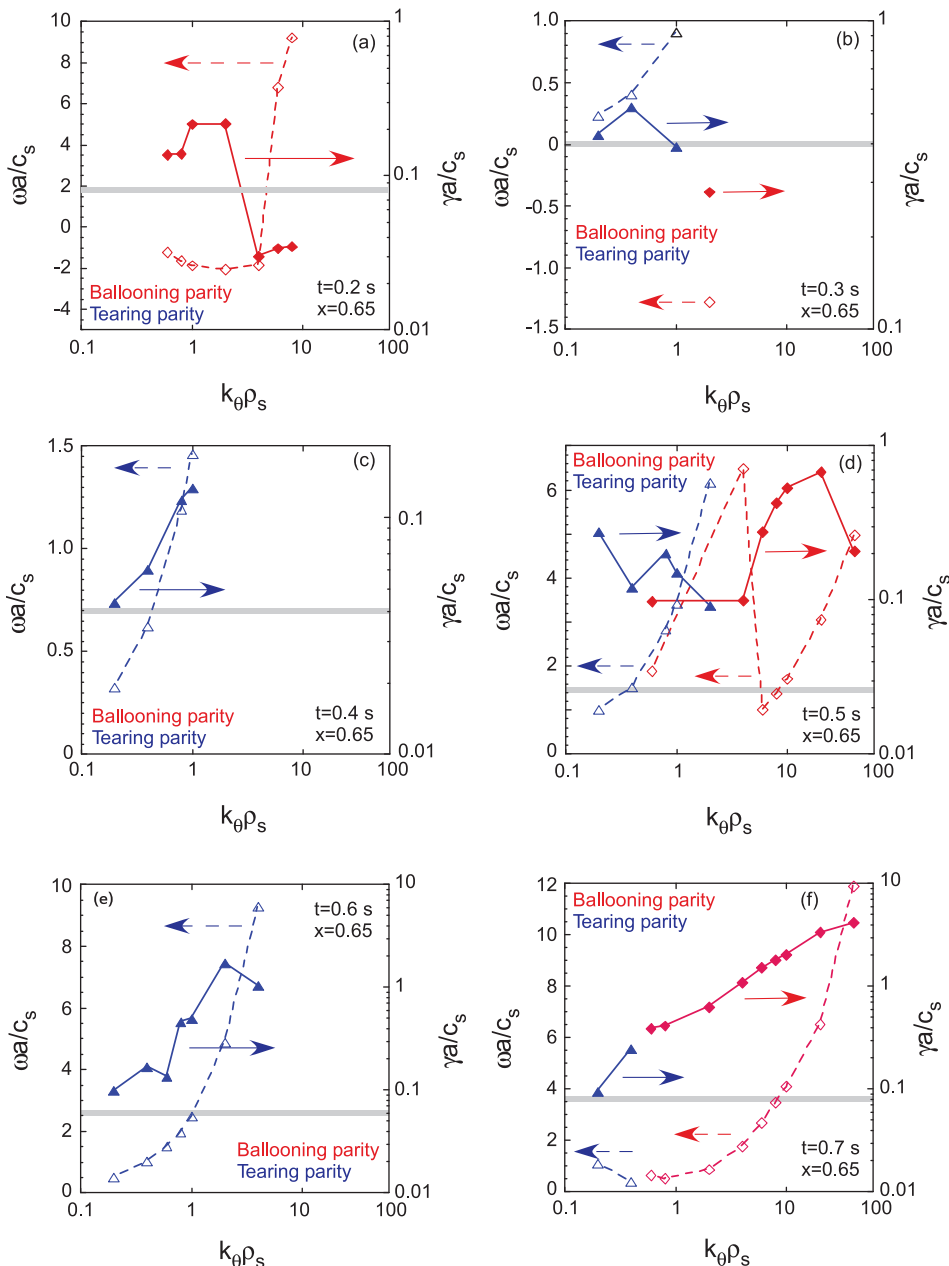


FIG. 5. Real frequencies and linear growth rates calculated from GYRO for the six different times (panels (a)–(f), respectively) at $x=0.6$. The gray horizontal shaded regions represent the ExB shearing rate as defined in the text.

The effect of the ExB shearing on the modes cannot practically be estimated until, again, full non-linear calculations are run, but it is probable that the ExB shearing suppresses the $k_{\theta}\rho_s \geq 4$ turbulence to some extent. That the electrostatic ballooning parity modes are the dominant ones at this time is consistent with the low β_e and with the large R/L_{T_i} and R/L_{T_e} drive terms.

With higher β_e , $\beta_e R/L_{T_e}$ and collisionality, microtearing modes are seen to dominate at $t=0.3$ s for $k_{\theta}\rho_s \leq 1$, with growth rates much greater than the ExB shearing rate (Fig. 5(b)). An ion direction ballooning parity mode (ITG) is seen to exist at $k_{\theta}\rho_s=2$, with a growth rate of comparable amplitude to the ExB shearing rate. No modes are calculated to be unstable for $k_{\theta}\rho_s > 2$. Similar behavior of modes is seen at $t=0.4$ s (Fig. 5(c)), with the microtearing dominant for $k_{\theta}\rho_s \leq 1$, and all modes are stable for $k_{\theta}\rho_s > 1$. Again, the linear growth rates exceed the ExB shearing rate. A scan of the input T_e gradient to the linear GYRO calculation was performed for this case to determine how far from threshold the experimental R/L_{T_e} is. For the fastest growing mode at $k_{\theta}\rho_s=1$, the microtearing linear threshold was determined to be at approximately 75% of the experimental value, which is outside the experimental uncertainty of R/L_{T_e} .

The α and R/L_{n_e} values at $t=0.5$ s, coupled with the higher β_e , $\beta_e R/L_{T_e}$ and ν_e^* values (Figs. 3(b) and 4(a)) suggested the possibility that a mixture of modes could exist at this time. This is indeed seen in Fig. 5(d), which gives the linear growth rates and real frequencies at this time. Microtearing is calculated to be the dominant mode for $k_{\theta}\rho_s \leq 2$, except for one wavenumber, $k_{\theta}\rho_s=0.6$, where an electron direction ballooning parity mode is calculated to be the fastest growing mode. This mixture of modes within this $k_{\theta}\rho_s$ range reflects the competition between modes for dominance, as discussed earlier in this section. For $k_{\theta}\rho_s \geq 4$, it is this ballooning parity mode that is dominant with modes predicted to be unstable up to the maximum $k_{\theta}\rho_s$ value, 40, that was studied. Parametric GYRO scans were carried out for selected $k_{\theta}\rho_s$ to identify the ballooning-parity modes at this time. At $k_{\theta}\rho_s=0.6$, the ballooning-parity mode was found to scale strongly with β , indicating a KBM. The experimental β was approximately 25% above the threshold beta for the KBM at this time. At higher $k_{\theta}\rho_s$, $k_{\theta}\rho_s=4$, the scaling of the linear growth rate with β was weak, but γ increased strongly with the temperature gradient, suggesting an ETG mode. For this $k_{\theta}\rho_s$ the experimental R/L_{T_e} was 25% greater than the threshold value. At $k_{\theta}\rho_s=20$, the mode is also identified as an ETG, with the experimental R/L_{T_e} 35%–40% above threshold.

Microtearing dominates across a wide range of $k_{\theta}\rho_s$ at $t=0.6$ s (Fig. 5(e)) with no ballooning parity modes predicted to be unstable. The mode is relatively far from marginal, with the experimental R/L_{T_e} for $k_{\theta}\rho_s=2$ being a factor to two greater than the linear threshold value. Consistent with the drop in β_e and increase in both R/L_{T_e} and especially R/L_{T_i} at $t=0.7$ s, the range of unstable microtearing modes shrinks, and that for electron direction ballooning parity modes increases, the latter covering the range of $k_{\theta}\rho_s$ from 0.6 to 40. This ballooning parity branch consists of different modes, similar to what was determined

for $t=0.5$ s. At $k_{\theta}\rho_s=0.6$, the mode is a KBM which is robustly unstable for a wide range of β . The mode at $k_{\theta}\rho_s=20$ is an ETG, with the experimental R/L_{T_e} over a factor of two above threshold. As a consistency check, the R/L_{T_e} at this time and at 0.5 s exceeds the analytic threshold value for ETG to be unstable.³² In all, the results of the linear growth rate calculations at $x=0.65$ are consistent with the expectations inferred from the parameter values and variations seen in Figs. 3 and 4, with electrostatic ballooning parity modes seen at the earliest and latest times, microtearing for the times in between, and some mixture of modes especially at $t=0.5$ s.

At $x=0.35$, microtearing modes are predicted to be unstable at low $k_{\theta}\rho_s$ (≤ 1) for $t=0.2$ – 0.5 s, although the linear growth rates are significantly lower (by 30%–50%) than the ExB shearing rate. At $t=0.6$ and 0.7 s, the microtearing mode at $k_{\theta}\rho_s \leq 1$ is supplanted by an ion-directed ballooning parity mode with growth rates of order 60%–70% of the ExB shearing rate.

The results for $x=0.5$ are similar to those discussed in detail for $x=0.65$. ITG-like modes are predicted to be dominant at $t=0.2$ s, with growth rates comparable to the ExB shearing rate, and microtearing is predicted to exist for $t \geq 0.3$ s at $k_{\theta}\rho_s \leq 1$, with at least some of the growth rates over the $k_{\theta}\rho_s$ range exceeding the shearing rate, except for $t=0.4$ and 0.5 s, where they are of order 50% of the ExB shearing rate. As for $x=0.65$, a mixture of microtearing and ballooning modes with significant linear growth rates is predicted to exist at $t=0.7$ s.

IV. REDUCED MODEL PREDICTIONS OF T_e

In Secs. II and III, it was established that while microtearing may not have an exclusive role in setting transport levels in the plasmas being studied, it certainly can have a very important and often dominant one. This was seen in both the parameter variations and the results of the linear growth rate calculations for the later times in the study. A complementary method of establishing the importance of microtearing in setting transport in this NSTX parameter regime is to compare measured temperature profiles with those predicted by a microtearing-based transport model. This is most easily done if there exists a reduced microtearing transport model that could be implemented in a predictive transport solver.

Such a model does exist. The Rebut-Lallia-Watkins (RLW) critical temperature gradient model^{29,30} is based on a scenario of magnetic turbulence affecting magnetic topology, which in turn drives plasma transport, and, in particular, electron transport. Specifically in this model, magnetic islands form and overlap when the electron temperature gradient exceeds a critical (threshold) value. It is the island overlap and resulting field line stochasticity (i.e., microtearing) that enhances the electron transport. In the model, the microtearing transport is reduced by high magnetic shear, which, according to the authors, leads to magnetic island sizes that are too small to be self-sustaining.

The critical electron temperature gradient for island overlap in this model is

$$\nabla T_{e,crit} \propto \left[\eta J B^3 / n_e T_e^{0.5} \right]^{0.5} \left(\frac{1}{q} \right), \quad (1)$$

where η is local plasma resistivity, J is current density, and q is the local q -value. For the NSTX discharge studied here, the measured electron temperature gradient exceeds the threshold value for all times and radial locations by between one and two orders of magnitude. Thus, for the case studied here, the electron temperature profiles are far from marginality and the transport is not stiff. This was found also for conventional aspect ratio tokamaks, specifically the OH and EC-heated TCV tokamak.³³

The electron thermal diffusivity for the RLW model is given by

$$\chi_{e,RLW} \propto \left[\left(\frac{\nabla T_e}{T_e} \right) + 2 \left(\frac{\nabla n_e}{n_e} \right) \right] \left(\frac{T_e}{T_i} \right)^{0.5} \left(\frac{R}{r} \right) (q^2 / \nabla q B R^{0.5}). \quad (2)$$

Note that while the microtearing transport level in this model is strongly dependent on n_e , T_e , T_i , q , and their gradients, there is no explicit or implicit dependence on either collisionality or β , which, from non-linear gyrokinetic calculations, are known to affect the microtearing-induced transport. These dependences are somewhat contained implicitly in the expression for the critical gradient given above, but this has virtually no effect on transport since the measured gradient is so much higher than the threshold value. The lack of ν_e^* and β_e dependences can certainly be viewed as a shortcoming in the model, and they should be taken into account in any future revision of this, or development of a new, microtearing-based reduced transport model.

For the study being presented here, the RLW model will be used to predict the time-evolving T_e profile, which will be compared to the measured profiles at the six times of interest. The RLW model has been implemented in the TRANSP code within the framework of the recently developed PT_SOLVER stiff transport solver. PT_SOLVER was implemented in TRANSP as an engine for predicting transport with stiff models such as TGLF. While RLW is not stiff, the PT_SOLVER option is still used for its prediction. The reason for this is that PT_SOLVER is a multi-region solver that offers the capability of employing different models, or user-defined input, in different regions of the plasma. The boundaries of the different regions can be defined by the user. For the case being presented here, the RLW model was used in the region from $x = 0.2$ to 0.8 . Inside $x = 0.2$, a user-defined χ_e value is used to reflect the enhanced electron transport associated with high-frequency Compressional/Global Alfvén activity which has been inferred for this region.³⁴ So far, no reduced model for this CAE/GAE-related transport has been developed. The $x = 0.8$ location has been chosen as the outer boundary. Beyond this location there are large uncertainties in the T_i profile data, as previously discussed.

For this calculation, only the T_e profile was predicted. At the early stages of any model testing, it is important to be able to isolate the effects of the model by studying predictions in as few transport channels as possible. This avoids

any non-linear propagation of prediction uncertainties that would occur when transport in multiple channels is being predicted, and thus could lead to misleading conclusions, either positive or negative. For instance, in this case study, the ions are governed primarily, but not exclusively, by neoclassical transport.²⁴ A prediction of the ion temperature profile using either neoclassical only or the RLW anomalous plus neoclassical models do not give precise agreement with the measured profiles. This difference propagates to and potentially confuses the comparison between predicted and measured T_e role, since the ion-electron coupling term is important for this case. Consequently, until there is a combined reduced anomalous plus neoclassical transport model that is valid for the parameter range of interest (validation studies of TGLF as applied to NSTX discharges are underway), and which can give an accurate prediction, the T_i profile for this calculation is taken to be the measured one. Similarly, the electron density, impurity density, and rotation profiles are also taken to be the measured ones.

Using the RLW model in the fashion described above, the comparisons between the predicted and measured electron temperature profiles are shown in Figs. 6(a)–6(f). In each of these figures, the solid line is the measured T_e while the dashed line is the predicted one. The shaded region represents the region in which the user-defined electron thermal diffusivity is applied. Here, χ_e is assumed to be $20 \text{ m}^2/\text{s}$ at $x = 0$ and linearly interpolated to match the $\chi_{e,RLW}$ value at $x = 0.2$, the innermost radius where the RLW model is used.

As can be seen in the figure at early times, where microtearing is not predicted to be unstable and/or is just becoming important ((a) and (b)), the model over predicts the T_e profile inside $x = 0.5$, and under predicts outside that radius. The agreement becomes much better as time progresses and as microtearing becomes dominant at low- k ($k_{\theta} \rho_s \leq 1$), with or without higher- k ballooning parity modes. By $t = 0.5 \text{ s}$, the agreement between the measured and predicted profiles can be considered to be quite good, except for inside $x = 0.2$ where the user-defined value is used. It is noted that even at $t = 0.6 \text{ s}$, where the MHD activity increases, and at $t = 0.7 \text{ s}$, after the possible H-L back transition at $T = 0.68 \text{ s}$, RLW is still doing a good job of predicting the measured T_e . The former implies that the MHD activity may be localized to near the plasma edge, while the latter implies that there is no significant change in the underlying transport levels on the time scale of 0.02 s , which is of order the electron confinement time (12–15 ms). The time evolution of the measured and predicted T_e values at $x = 0.35$, 0.50 , and 0.65 is shown in Fig. 7. From this figure also, the large differences between the measured and predicted T_e profiles at early times shrinks as time progresses. The predicted T_e value at $x = 0.65$ is typically 10% lower than the measured value at $t = 0.5 \text{ s}$. As mentioned previously, the uncertainty in the measured T_e value is typically between 2% and 3%. Typical $\chi_{e,RLW}$ values at $x = 0.35$ – 0.65 are $\sim 8 \text{ m}^2/\text{s}$, consistent with the values inferred from interpretive TRANSP analysis. At early times ($t = 0.2$ – 0.4 s), the $\chi_{e,RLW}$ values can range up to $\sim 20 \text{ m}^2/\text{s}$ near $x = 0.3$.

The standard profile fit metrics between the predicted and the experimental profiles are given in Table I for the six times of interest. The profile metrics are defined below:

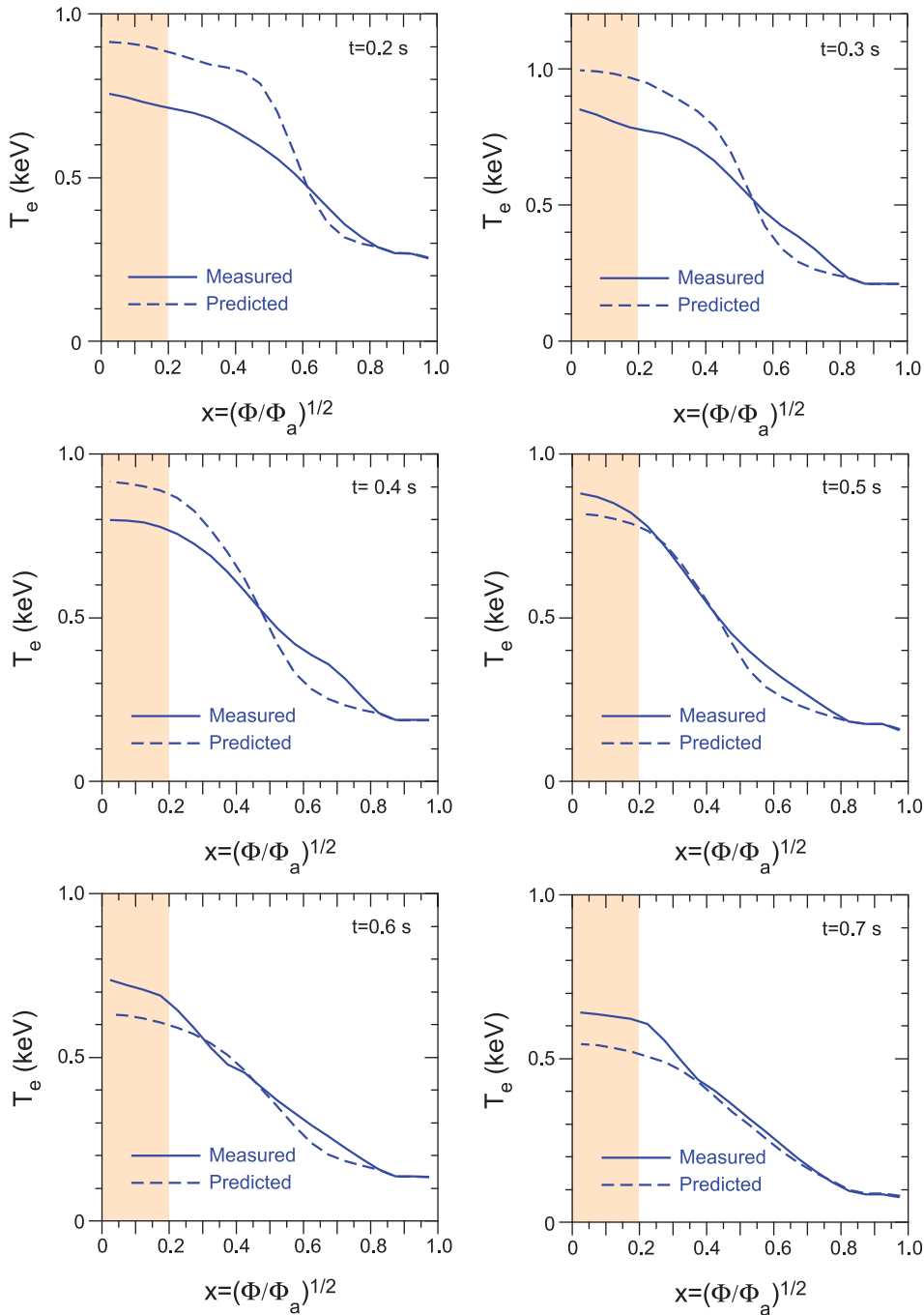


FIG. 6. Measured T_e profiles (solid lines) and those predicted using the RLW model (dashed lines) compared for the six times of interest. The shaded region inside of $x = 0.2$ indicates where a user-defined χ_e is applied. The outer boundary for using the RLW model is $x = 0.8$.

RMS Deviation

$$\sigma = \sqrt{\frac{1}{N} \sum_{i=1}^N \epsilon_j^2}. \quad (3)$$

Offset

$$f = \frac{1}{N} \sum_{i=1}^N \epsilon_j, \quad (4)$$

where

$$\epsilon_j = \frac{T_{pred,j} - T_{exp,j}}{\max(T_{exp,j})}. \quad (5)$$

For the calculation of the metrics, only profile values between $x = 0.2$ and 0.8 were used; this was the range in which the RLW model was applied. It is clearly seen in the table that the RMS deviation decreases dramatically with time, a quantitative indication of the improvement in the goodness of fit of the RLW model. For the last four times of interest, $\sigma = 6$ to 11% . This compares favorably with the RMS deviation of 6% – 14% for the TGLF model over a range of DIII-D discharge types.³⁵

The RLW model does a reasonably good job in predicting the T_e profile for this high ν_e^* plasma where microtearing is expected and calculated to be important, thus the use of this model is justified, at least for the later times. It is useful to make a similar prediction for comparison, however, using RLW for a plasma where microtearing is not believed to be

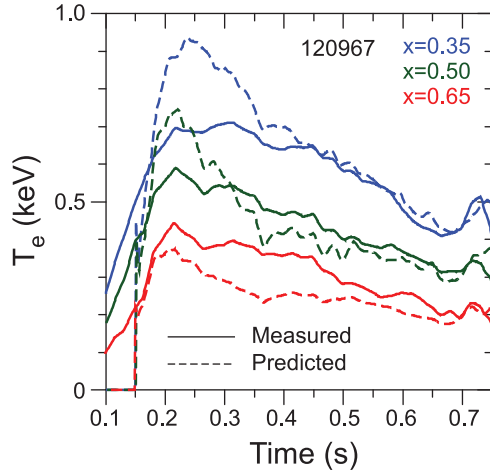


FIG. 7. Measured T_e profiles (solid lines) and those predicted using the RLW model (dashed lines) as functions of time for the three radial locations.

TABLE I. T_e profile fit metrics for the six times of interest.

Time of interest (s)	RMS deviation (%)	Offset (%)
0.2	46	44
0.3	16	6
0.4	11	0
0.5	7	-6
0.6	9	-7
0.7	6	-5

important. Such a result is shown in Figs. 8(a) and 8(b). The discharge shown in the figure was taken from a scan of pre-shot lithium deposition, which was used for wall conditioning. For this discharge, $I_p = 0.8$ MA, $B_T = 0.44$ T, and $\kappa = 1.8$. This particular discharge had a large amount of lithium applied pre-shot, close to 1 gm, and was at the lower range of collisionality. $\nu_e^* \sim 0.06$ at $x = 0.5$ in this discharge, as compared to ≥ 0.20 in 120967. Fig. 8(a) shows the linear growth rate (in units of c_s/a) of the fastest growing mode as calculated by GYRO across the outer radii of the plasma. Here, $\rho = r/a$. The dominant mode for this case during the “steady-state” portion of the plasma is a ballooning parity hybrid mode, with characteristics of both TEM and KBM. The growth rate exceeds the ExB shearing rate at all radii for

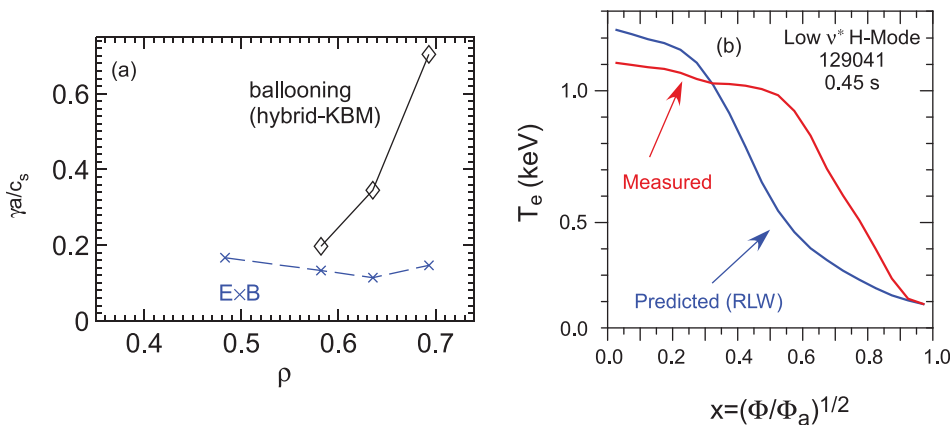


FIG. 8. Measured T_e profile (solid line) and one predicted using the RLW model (dashed line) for a low collisionality discharge.

which the mode is calculated to be unstable. Not surprisingly, when the RLW model is used to predict the T_e profile in this plasma in which microtearing is subdominant or stable, the agreement is poor, as can be seen in Fig. 8(b). It is seen that the measured T_e profile is much broader than that predicted by the model, which under predicts the T_e outside of $x = 0.3$ by up to a factor of two.

The region of applicability of RLW can be assessed further by examining the variation of total electron stored energy. The electron stored energy, as given by RLW, goes as³⁰

$$W_e = 0.026n_e^{0.75}Z_{eff}^{0.25}B_T^{0.5}I_p^{0.5}(Ra^2\kappa)^{11/12} + 0.012I_p(Ra^2\kappa)^{0.5}P_{tot}/Z_{eff}^{0.5}, \quad (6)$$

in units of MJ, 10^{19} m⁻³, T, MA, m, and MW. As admonished even by the RLW authors, this scaling should be used only as a guide. To this end, the ratio of the experimental electron stored energy to that predicted by RLW is plotted in Fig. 9 as a function of electron collisionality at $x = 0.5$. The data points are taken from a collection of H-mode discharges consisting of those using either HeGDC + boronization or lithium evaporation for wall conditioning. The details of the datasets can be found in Kaye *et al.*²⁵ For the plot shown here, the data are constrained so that $q(x = 0.5) = 1.75 - 3.0$ to avoid any implicit dependence on q that had not been identified.³⁰ The data were divided into three categories based on ELM activity: ELM-free (blue), giant ELMs (green), and small ELMs (red). The ratio $W_e/W_{e,RLW}$ varies from ~ 2.0 at the lowest collisionality to ~ 1.0 at the highest. Note that the discharge 120967 used for this case study had a $q(x = 0.5)$ value that was greater than the range constraint presented in the figure, so this discharge is not included in this collection of data. While there certainly are dependences in the overall ratio due to the different effects of the various ELM types, the overall trend is that the ratio tends towards ~ 1.0 as collisionality increases. This is consistent with the trends predicted by the non-linear gyrokinetic analysis^{21,25} indicating the greater role of microtearing at the higher collisionalities in this collection of discharges. The trend and energy ratio values at the higher collisionalities indicate the relevance of using the RLW model in this parameter regime.

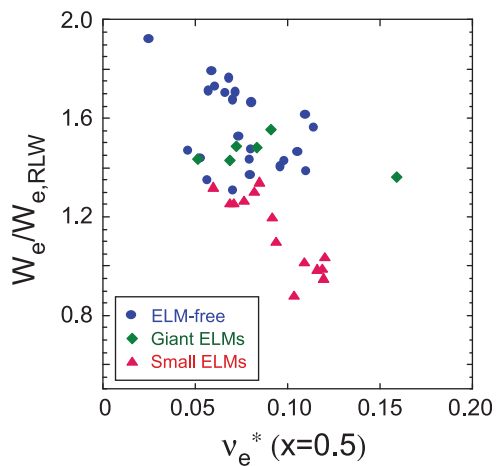


FIG. 9. Measured electron stored energy normalized to the electron stored energy predicted by RLW vs electron collisionality at $x = 0.5$.

V. SUMMARY AND DISCUSSION

In this paper, a particular discharge was used as a case study for predicting the time evolution of the electron temperature using a reduced model that reflects microtearing-driven transport. The evolution of various discharge parameters representing the possible importance of various microinstabilities was first tracked, and this was followed by a determination of the linear (micro-)stability properties using the GYRO gyrokinetic code. Not surprisingly, the implications of the parameter evolution and the linear stability calculations were consistent. These results suggested the importance of ∇T_e and/or ∇T_i -driven electrostatic modes in the plasma core early in the discharge when β_e and ν_e^* are relatively low, but a growing importance of microtearing-dominated transport with advancing time as β_e and ν_e^* increased. It was also found that ballooning parity modes (ITG/TEM/KBM/ETG) can also play a role, even at later times in the discharge.

A microtearing based reduced transport model developed in the mid-1980s, the Rebut-Lallia-Watkins model, was then used as a basis for predicting the electron temperature profile evolution in the plasma, using the measurements for all other profiles. This model was found to do a reasonable job of predicting the measured T_e profiles in the regions and at the times where microtearing is expected to be important. Shortcomings of the model include a lack of any collisionality or β dependence, which are known to affect microtearing stability, but nevertheless the model does well even during discharge times where the edge MHD activity is slightly enhanced and shortly after an H-L back transition. The value of χ_e predicted by the model at a particular time and location at which the non-linear transport level was calculated by GYRO agrees with the non-linear prediction.

Another microtearing-based transport model that could potentially be tested is that given by Wong *et al.*²³ Calculations of the electron thermal diffusivity from this model indicate not as good agreement with the experimentally inferred χ_e profile as does the RLW χ_e for the specific discharge being studied. The Wong model showed significant departures from the experimentally inferred χ_e except in the mid radius ($x \sim 0.5$) region. Consequently, the predictions

were restricted to use of the RLW model, which showed better agreement with the experimental χ_e .

There are two coupled key points of emphasis that stem from this work. The first is that the prediction, and the agreement that was obtained, is by no means universal or extrapolatable in a simple manner. The discharge used for this case study was comprehensively analyzed through previous gyrokinetic simulations, and the importance of microtearing was established. This first point leads to the second, which is that use of any reduced model has to be justified. It is essential to know whether the physics represented by the model is valid for the regime being explored. This can be done, for instance, by independent calculations such as the linear gyrokinetic result presented in Sec. III. While good agreement was found in the case study discharge and other discharges where microtearing was predicted to be unstable and important, the agreement was poor for plasmas where microtearing was predicted to be stable or subdominant.

Consequently, it would not be justifiable to simply apply the RLW model for predicting T_e in, for instance, NSTX-U scenarios, or regimes in other devices, where collisionality may be lower and microtearing may be subdominant. Model validation in one regime does not necessarily imply validity in another, and this presents a certain paradox. Using a simple, reduced predictive tool is justifiable if it is known a priori that the physics of the predicted scenario is compatible with that of the model, but the microstability characteristics of the future scenario depends on the results from use of the predictive models. Some justification of the model use can be grounded in an a posteriori assessment of the stability properties of the predicted regime, although not with certainty. If the predicted regime is found to be stable to the modes driving the prediction, an inconsistency and lack of justification for use of the model are easily identified. However, any “self-consistency” found in the predicted parameter regime may merely be a “self-fulfilling prophecy.” Predicted profiles may indeed suggest the validity of a model in that gyrokinetic calculations might support the underlying physics assumptions of the model used to produce them, but that self-consistency does not necessarily imply accuracy. While this leaves this particular predictive methodology in somewhat of an uncertain state, it is, nevertheless, a reality that must be recognized. The best approach appears to be to develop a reduced model from detailed gyrokinetic calculations that can encompass as much of the fundamental physics as possible, in the manner that TGLF was developed. Work is underway to explore the validity of this particular model for the range of presently accessible ST parameter regimes.

ACKNOWLEDGMENTS

This work has been supported by U.S. Department of Energy Contract DE-AC02-09CH11466.

¹J. Candy and R. Waltz, *J. Comput. Phys.* **186**, 545 (2003).

²W. Wang, Z. Lin, W. M. Tang, W. W. Lee, S. Ethier, J. Lewandowski, G. Rewoldt, T. S. Hahn, and J. Manickam, *Phys. Plasmas* **13**, 092505 (2006).

³A. G. Peeters, Y. Camenen, F. J. Casson, W. A. Hornsby, A. P. Snodin, D. Strintzi, and G. Szepesi, *Comput. Phys. Commun.* **180**, 2650 (2009).

⁴Y. Chen and S. E. Parker, *J. Comput. Phys.* **220**, 839 (2007).

- ⁵F. Jenko, W. Dorland, M. Kotschenreuther, and B. N. Rogers, *Phys. Plasmas* **7**, 1904 (2000).
- ⁶M. Kotschenreuther, G. Rewoldt, and W. M. Tang, *Comput. Phys. Commun.* **88**, 128 (1995).
- ⁷N. T. Howard, A. E. White, M. Greenwald, C. Holland, and J. Candy, *Phys. Plasmas* **21**, 032308 (2014).
- ⁸W. M. Tang, *Nucl. Fusion* **26**, 1605 (1986).
- ⁹F. M. Poli, private communication (2014).
- ¹⁰F. M. Poli, C. E. Kessel, M. S. Chance, S. C. Jardin, and J. Manickam, *Nucl. Fusion* **52**, 063027 (2012).
- ¹¹M. Erba, *Plasma Phys. Controlled Fusion* **39**, 261 (1997).
- ¹²F. D. Halpern, A. Eriksson, G. Bateman, A. Kritz, A. Pankin, C. Wolfe, and J. Weiland, *Phys. Plasmas* **15**, 012304 (2008).
- ¹³R. E. Waltz, G. M. Staebler, W. Dorland, G. W. Hammett, M. Kotschenreuther, and J. A. Konings, *Phys. Plasmas* **4**, 2482 (1997).
- ¹⁴G. M. Staebler, J. E. Kinsey, and R. E. Waltz, *Phys. Plasmas* **14**, 055909 (2007).
- ¹⁵J. E. Kinsey, G. M. Staebler, J. Candy, R. E. Waltz, and R. V. Budny, *Nucl. Fusion* **51**, 083001 (2011).
- ¹⁶C. Holland, L. Schmitz, T. Rhodes, W. A. Peebles, J. C. Hillesheim, G. Wang, L. Zeng, E. J. Doyle, S. P. Smith, R. Prater, K. H. Burrell, J. Candy, R. E. Waltz, J. E. Kinsey, G. M. Staebler, J. C. DeBoo, C. C. Petty, G. R. McKee, Z. Yan, and A. E. White, *Phys. Plasmas* **18**, 056113 (2011).
- ¹⁷R. V. Budny, *Nucl. Fusion* **49**, 085008 (2009).
- ¹⁸R. V. Budny, private communication (2014).
- ¹⁹R. D. Hazeltine, D. Dobrot, and T. S. Wang, *Phys. Fluids* **18**, 1778 (1975).
- ²⁰W. G. Guttenfelder, J. Candy, S. M. Kaye, W. M. Nevins, R. E. Bell, G. W. Hammett, B. P. LeBlanc, and H. Yuh, *Phys. Plasmas* **19**, 022506 (2012).
- ²¹W. G. Guttenfelder, J. Candy, S. M. Kaye, W. M. Nevins, E. Wang, J. Zhang, R. E. Bell, N. A. Crocker, G. W. Hammett, B. P. LeBlanc, D. R. Mikkelsen, Y. Ren, and H. Yuh, *Phys. Plasmas* **19**, 056119 (2012).
- ²²D. J. Applegate, C. M. Roach, S. C. Cowley, W. D. Dorland, N. Joiner, R. J. Akers, N. J. Conway, A. R. Field, A. Patel, M. Valovic, and M. J. Walsh, *Phys. Plasmas* **11**, 5085 (2004).
- ²³K.-L. Wong, S. Kaye, D. R. Mikkelsen, J. A. Krommes, K. Hill, R. Bell, and B. LeBlanc, *Phys. Plasmas* **15**, 056108 (2008).
- ²⁴S. M. Kaye, F. M. Levinton, D. Stutman, K. Tritz, H. Yuh, M. G. Bell, R. E. Bell, C. W. Domier, D. Gates, W. Horton, J. Kim, B. P. LeBlanc, N. C. Luhmann, Jr., R. Maingi, E. Mazzucato, J. E. Menard, D. Mikkelsen, D. Mueller, H. Park, G. Rewoldt, S. A. Sabbagh, D. R. Smith, and W. Wang, *Nucl. Fusion* **47**, 499 (2007).
- ²⁵S. M. Kaye, S. Gerhardt, W. Guttenfelder, R. Maingi, R. E. Bell, A. Diallo, B. P. LeBlanc, and M. Podesta, *Nucl. Fusion* **53**, 063005 (2013).
- ²⁶W. G. Guttenfelder, J. L. Peterson, J. Candy, S. M. Kaye, Y. Ren, R. E. Bell, G. W. Hammett, B. P. LeBlanc, D. R. Mikkelsen, W. M. Nevins, and H. Yuh, *Nucl. Fusion* **53**, 093022 (2013).
- ²⁷J. E. Menard, S. Gerhardt, M. Bell, J. Bialek, A. Brooks, J. Canik, J. Chrzanowski, M. Denault, L. Dudek, D. Gates, N. Gorelenkov, W. Guttenfelder, R. Hatcher, J. Hosea, R. Kaita, S. Kaye, C. Kessel, E. Kolemen, H. Kugel, R. Maingi, M. Mardenfeld, D. Mueller, B. Nelson, C. Neumeyer, M. Ono, E. Perry, R. Ramakrishnan, R. Raman, Y. Ren, S. Sabbagh, M. Smith, V. Soukhanovskii, T. Stevenson, R. Strykowski, D. Stutman, G. Taylo, P. Titus, K. Tresemer, K. Tritz, M. Viola, M. Williams, R. Woolley, H. Yuh, H. Zhang, Y. Zhai, A. Zofaghari, and the NSTX Team, *Nucl. Fusion* **52**, 083015 (2012).
- ²⁸J. E. Menard, L. Bromberg, T. Brown, T. Burgess, D. Dix, L. El-Guebaly, T. Gerrity, R. J. Goldston, R. J. Hawryluk, R. Kastner, C. Kessel, S. Malang, J. Minervini, G. H. Neilson, C. L. Neumeyer, S. Prager, M. Sawan, J. Sheffield, A. Sternlieb, L. Waganer, D. Whyte, and M. Zarnstorff, *Nucl. Fusion* **51**, 103014 (2011).
- ²⁹P. H. Rebut and M. Brusati, *Plasma Phys. Controlled Fusion* **28**, 113 (1986).
- ³⁰P. H. Rebut, P. P. Lallia, and M. L. Watkins, "The critical temperature gradient model of plasma transport: applications to JET and future tokamaks," in Proceedings of the 12th IAEA Conference on Plasma Physics and Controlled Nuclear Fusion Research, Nice, France, 1988, IAEA-CN-50/D-4-1.
- ³¹R. L. Miller, M. S. Chu, J. M. Greene, Y. R. Lin-Liu, and R. E. Waltz, *Phys. Plasmas* **5**, 973 (1998).
- ³²F. Jenko, W. Dorland, and G. W. Hammett, *Phys. Plasmas* **8**, 4096 (2001).
- ³³C. Angioni, "Modelling of electron transport and of sawtooth activity in tokamaks," Ph.D. dissertation (Ecole Polytechnique Fédérale de Lausanne EPFL, 2001).
- ³⁴D. Stutman, L. Delgado-Aparicio, N. Gorelenkov, M. Finkenthal, E. Fredrickson, S. Kaye, E. Mazzucato, and K. Tritz, *Phys. Rev. Lett.* **102**, 115002 (2009).
- ³⁵G. M. Staebler and J. E. Kinsey, *Phys. Plasmas* **17**, 122309 (2010).